PHYSICAL REVIEW B **84**, 085445 (2011)

Current-induced energy barrier suppression for electromigration from first principles

Ruoxing Zhang,[1,2] Ivan Rungger,[2] Stefano Sanvito,[2] and Shimin Hou[1,*]
[1]*Key Laboratory for the Physics and Chemistry of Nanodevices, Department of Electronics, Peking University, Beijing 100871, China*
[2]*School of Physics and CRANN, Trinity College, Dublin 2, Ireland*
(Received 13 June 2011; published 29 August 2011)

We present an efficient method for evaluating current-induced forces in nanoscale junctions, which naturally integrates into the nonequilibrium Green's function formalism implemented within density functional theory. This allows us to perform dynamic atomic relaxation in the presence of an electric current while evaluating the current–voltage characteristics. The central idea consists of expressing the system energy density matrix in terms of Green's functions. To validate our implementation, we perform a series of benchmark calculations, both at zero and at finite bias. First we evaluate the current-induced forces acting over an Al nanowire and compare them with previously published results for fixed geometries. Then we perform structural relaxation of the same wires under bias and determine the critical voltage at which they break. We find that although a perfectly straight wire does not break at any of the voltages considered, a zigzag wire is more fragile and snaps at 1.4 V, with the Al atoms moving against the electron flow. The critical current density for the rupture is estimated to be 9.6×10^{10} A/cm^2, in good agreement with the experimentally measured value of 5×10^{10} A/cm^2. Finally, we demonstrate the capability of our scheme to tackle the electromigration problem by studying the current-induced motion of a single Si atom covalently attached to the sidewall of a (4,4) armchair single-walled carbon nanotube. Our calculations indicate that if Si is attached along the current path, then current-induced forces can induce migration. In contrast, if the bonding site is away from the current path, then the adatom remains stable regardless of the voltage. An analysis based on decomposing the total force into a wind and an electrostatic component, as well as on a detailed evaluation of the bond currents, shows that this remarkable electromigration phenomenon is due solely to the position-dependent wind force.

DOI: 10.1103/PhysRevB.84.085445 PACS number(s): 85.65.+h, 73.40.Jn, 73.40.Cg, 73.40.Gk

I. INTRODUCTION

In recent years, nanoscale devices have attracted increasing attention. The interest is motivated by their potential as a viable technology for either extending or replacing the conventional Si metal-oxide-semiconductor field-effect transistor (MOSFET) platform.[1,2] However, as the device size shrinks, atomic rearrangements[3–7] and diffusion of atoms[8–12] in the presence of electric currents become key problems, limiting the device's mechanical stability and the persistence in time of uniform electron transport properties. These issues are closely related to the presence of current-generated forces acting on the nuclei. The interaction between current-carrying electrons and ions manifests itself in two ways: as local ionic heating and as current-induced forces.[13–15] Certainly both may have significant effects on the atomic and electronic structure of a nanoscale junction.[13–23] Local heating involves a series of inelastic transitions among states of different energy; thus, it is associated with the excitations of the corresponding vibrational modes. Current-induced forces, in contrast, mainly arise from the charge density redistribution caused by the electron flow. In a pictorial way, this force is analogous to the one exerted by the running water of a river on the stones in its bank and is usually referred to as the wind force.

In a quasiballistic transport regime, the one investigated here, local ionic heating is small and usually gives an insignificant contribution to the atomic motion.[15] But what about current-induced forces? Interestingly, the typical current densities in nanoscale junctions are much larger than those in the conducting interconnects widely used in solid-state circuits. Because current-induced electromigration is already one of the major causes of device failure in microelectronics,[24–27] we expect that current-induced forces in nanodevices will play an even more important role in limiting their structural stability. This clearly indicates that a deep understanding of current-induced forces may help us in the design of more robust devices, possibly with longer lifetimes. Furthermore, we can speculate about using current-induced forces to operate a device, e.g., as a tool for switching a resistor between different resistance values, or to assemble devices by drifting atoms at desired positions with electric currents.

Despite their importance, to our knowledge, only a few fundamental studies[14,28] have focused on the implementation of current-induced forces in a practical algorithm. Furthermore, much remains to be understood about the electromigration process and the calculations of diffusion paths. With these two goals in mind, we have developed an efficient computational scheme for the calculation of forces at finite bias and implemented it in the *ab initio* electronic transport code Smeagol.[29–31] Smeagol is based on the nonequilibrium Green's function (NEGF) method,[32–34] and it is interfaced with the localized atomic orbital pseudopotential code Siesta,[35,36] from which it obtains the density functional theory (DFT) Hamiltonian matrix. Such an implementation based on the ground state DFT exchange-correlation functionals corresponds to the special case in which the NEGF scheme is applied within a mean field single particle approximation. As such, the method is equivalent to single particle scattering theory. To maintain consistency with a large body of existing literature, we still refer to our method as the NEGF + DFT. Our scheme enables us to perform structural relaxation at finite bias and at the same time monitor the device current–voltage

 ©2011 American Physical Society

(I-V) characteristics. Furthermore, it potentially opens up the possibility of performing molecular dynamics simulations under electron current flow conditions.

The implementation of current-induced forces is a rather challenging task, because it involves the evaluation of the atomic forces in a nonequilibrium situation, where the total number of electrons in the simulation cell is not guaranteed and the total energy is not defined. For a closed, finite, and time-independent system at equilibrium, the atomic forces are well defined and can be obtained from the conventional Hellmann-Feynman (HF) theorem.[37] In contrast, for an open and out-of-equilibrium situation, we are no longer able to define the atomic forces from such a classical energy perspective, and an alternative strategy is needed. To our knowledge, there are two starting points in the derivation of the atomic forces under the presence of a current. The first starts from a time-dependent Lagrangian mean-field theory,[38,39] and the second is completely based on quantum-mechanical many-body dynamic theory.[40] By using this second strategy, it is possible to define the atomic forces for a general quantum mechanical system as the time derivative of the expectation value of the ionic momentum operators.[15,28] The method holds true for the time-dependent situation as well. Although the physical origin and the formal definition of current-induced forces seem rather clear, in the past there has been some controversy over whether or not such forces are conservative.[41] More recently, the controversy seems to have pointed toward the nonconservative nature of current-induced forces.[7,42]

Our paper is organized as follows. In the next section, we briefly introduce our computational methodology and the technical implementations adopted in Smeagol. Then we present a series of test cases for atomic forces calculated either at zero or at finite bias. In the finite-bias calculations, we choose a capacitor setup, where the electrodes are completely disconnected so that no current flows. Such a setup allows us to verify the correctness of the NEGF-calculated electrostatic forces, because these can be compared to those obtained by a corresponding DFT total energy calculation, including a finite electric field.[35,36] We then present an investigation on the current-induced forces acting on Al point contacts and compare the results to previous calculations for similar systems, where jellium leads were used. We also determine the critical bias leading to junction breaking for straight and zigzag wires, finding a rather good agreement with available experimental results. In the last section, we present a series of numerical calculations demonstrating the capability of our implementation to tackle the electromigration phenomenon. Our test case is that of one Si adatom drifting along the path of the current in the vicinity of a (4,4) armchair single-walled carbon nanotube (SWCNT).

II. METHODS

To define the atomic forces acting on a system sustaining a steady-state electric current, we first provide a brief overview of the transformed HF theorem, which relates conservative atomic forces to classical energies. The HF theorem expresses the total force acting on the Ith atom $\vec{F}_I$ as the negative derivative of the total energy E with respect to its position $\vec{R}_I$:

$$\begin{aligned}\vec{F}_I &= -\frac{\partial E(\vec{R}_I)}{\partial \vec{R}_I} \\ &= -\frac{\partial \langle\Psi|\,\hat{H}(\vec{R}_I)\,|\Psi\rangle}{\partial \vec{R}_I} \\ &= \left[-\langle\Psi|\frac{\partial \hat{H}(\vec{R}_I)}{\partial \vec{R}_I}|\Psi\rangle\right] \\ &\quad + \left[-\left\langle\frac{\partial\Psi}{\partial\vec{R}_I}\right|\hat{H}(\vec{R}_I)|\Psi\rangle - \langle\Psi|\hat{H}(\vec{R}_I)\left|\frac{\partial\Psi}{\partial\vec{R}_I}\right\rangle\right]. \end{aligned} \quad (1)$$

Here, $\hat{H}(\vec{R}_I)$ is the many-electron Hamiltonian operator and $|\Psi\rangle$ is the associated many-electron normalized wave function. The first term in the last equality of Eq. (1) is the well-known conventional HF force, and the second term is often referred to as the Pulay force.[43] This vanishes only if $|\Psi\rangle$ is an exact eigenstate of $\hat{H}$ or if the basis set does not depend parametrically on the ionic coordinates (as for a plan-wave basis set).[28] In that particular case, Eq. (1) reduces to the conventional HF theorem.

In DFT, the ground state total energy is a well-defined quantity. As such, the atomic forces can be calculated by taking explicitly the derivative of the total energy with respect to the atomic positions, as written in the first equality of Eq. (1). This is well documented, and a detailed description of the implementation used in Siesta can be found in Refs. 35,36, and 44. The result can be generally written as the sum of two terms:

$$\vec{F} = \vec{F}_{BS} + \vec{F}_C. \quad (2)$$

Here $\vec{F}_{BS} = -\partial E_{BS}/\partial \vec{R}_I$ describes the force originating from the band structure (BS) contribution of the total DFT energy E_{BS}, which is equal to the sum of the eigenvalues of the occupied states. The second term $\vec{F}_C$ is obtained by taking the derivative of the remaining contributions to the DFT total energy.[44] The force given in Eq. (2) automatically includes the Pulay corrections arising because of the employed numerical local orbital basis set. The Kohn-Sham (KS) equation of the system reads[36]

$$\sum_{\upsilon} H_{\mu\upsilon}\psi_{i\upsilon} = \varepsilon_i \sum_{\upsilon} S_{\mu\upsilon}\psi_{i\upsilon}, \quad (3)$$

where $H_{\mu\upsilon}$ is the KS-Hamiltonian matrix element, $S_{\mu\upsilon}$ is the overlap matrix element, ε_i is the ith KS eigenvalue, $\psi_{i\mu}$ is the corresponding eigenvector, and the indices μ and ν label the local orbital basis set. The density matrix of the system $\rho_{\mu\upsilon}$ is then defined as

$$\rho_{\mu\upsilon} = \sum_i f(\varepsilon_i)\psi_{i\mu}\psi^*_{i\upsilon}, \quad (4)$$

where $f(\varepsilon_i)$ is the occupation probability of the state having ε_i as its KS eigenvalue. In our case, $f(\varepsilon_i)$ is the Fermi-Dirac distribution. The BS force $\vec{F}_{BS}$ can then be written as

$$\vec{F}_{BS} = -\sum_{\mu\upsilon}\rho_{\mu\upsilon}\frac{\partial H_{\upsilon\mu}}{\partial \vec{R}_I} + \sum_{\mu\upsilon}\Omega_{\mu\upsilon}\frac{\partial S_{\upsilon\mu}}{\partial \vec{R}_I}, \quad (5)$$

where $\Omega_{\mu\upsilon}$ is the so-called energy density matrix,[44] defined as

$$\Omega_{\mu\upsilon} = \sum_i \varepsilon_i f(\varepsilon_i)\psi_{i\mu}\psi^*_{i\upsilon}. \quad (6)$$

Because our interest is in extending the formalism to open systems described by the NEGF formalism,[30] it is convenient to rewrite Eqs. (4) and (6) in terms of the retarded Green's function $G_{\mu\upsilon}(E) = [(E + i\delta)S - H]^{-1}_{\mu\upsilon}$, with δ being a small positive number. The Eq. (4) can then be recasted as the energy integral[30]

$$\rho_{\mu\upsilon} = -\frac{1}{2\pi i}\int_{-\infty}^{\infty}[G_{\mu\upsilon}(E) - G^\dagger_{\mu\upsilon}(E)]f(E)\,dE, \quad (7)$$

and it is straightforward to show that a similar expression holds for the energy density matrix:

$$\Omega_{\mu\upsilon} = -\frac{1}{2\pi i}\int_{-\infty}^{\infty}E(G_{\mu\upsilon}(E) - G^\dagger_{\mu\upsilon}(E))f(E)\,dE. \quad (8)$$

The only difference between Eqs. (7) and (8) is the additional factor E appearing in the integrand. The advantage of expressing the forces in terms of Green's functions is that we can extend the formalism to open systems.

We now move to define the forces for a system out of equilibrium and sustaining a steady-state current. In this situation, the HF theorem is not directly applicable.[15,28,45,46] However, Di Ventra and co-workers have shown that the forces can be defined in a more general way, i.e., as the time derivative of the expectation value of the ionic momentum operator,[15,28] namely

$$\vec{F}_I = \frac{\partial}{\partial t}\langle\Psi(t)| - i\hbar\frac{\partial}{\partial\vec{R}_I}|\Psi(t)\rangle, \quad (9)$$

where the wave function is in general time dependent. Based on Eq. (9) and the more restrictive condition for the wave function[28]

$$\langle\Psi(t)|\hat{H} - i\hbar\frac{\partial}{\partial t}|\Psi(t)\rangle = 0, \quad (10)$$

by some algebraic manipulations, we eventually derive an Ehrenfest-like expression for the forces that applies to a generic time-dependent problem expanded over a finite basis set:

$$\vec{F}_I = -\left[\langle\Psi(t)|\frac{\partial\hat{H}}{\partial\vec{R}_I}|\Psi(t)\rangle + \left\langle\frac{\partial\Psi(t)}{\partial\vec{R}_I}\right|\hat{H} - i\hbar\frac{\partial}{\partial t}|\Psi(t)\rangle + \left\langle\frac{\partial\Psi(t)}{\partial\vec{R}_I}\right|\hat{H} - i\hbar\frac{\partial}{\partial t}|\Psi(t)\rangle^*\right], \quad (11)$$

For steady-state transport problems, the wave function of the system can be written as $|\Psi(t)\rangle = e^{-iEt/\hbar}|\psi\rangle$, where E is a phase factor with units of energy. By using this result and Eq. (11), a final form for the total atomic forces in a system with steady-state electric current flow is given as

$$\vec{F}_I = -\frac{\partial\,\langle\psi|\,\hat{H}\,|\psi\rangle}{\partial\vec{R}_I}. \quad (12)$$

At this point, we want to stress that Eq. (12) is formally identical to the HF force given in Eq. (1), although the two equations are based on a completely different derivation, and Eq. (12) holds under more general conditions. Because of this formal analogy, however, the expression in Eq. (2), derived for a closed system at equilibrium, is also valid for the steady-state transport problem, which is explored here. All terms contained in $\vec{F}_C$ depend entirely on the charge density matrix $\rho_{\mu\upsilon}$ (Refs. 35 and 44). This means that the forces can be computed exactly as in a standard DFT ground state calculation once the nonequilibrium $\rho_{\mu\upsilon}$ is known. Therefore, in the remaining part of this section, we focus on detailing how $\rho_{\mu\upsilon}$ and $\Omega_{\mu\upsilon}$ are extracted in the nonequilibrium case.

The NEGF scheme implemented in Smeagol is based on dividing a two-terminal device into three parts: the semi-infinite left and right electrodes (the leads) and the scattering region (or the extended molecule).[30] The effects of the leads on the scattering region are taken into account via the energy-dependent self-energies and the associated coupling matrices: $\Gamma_{L\mu\upsilon}(E)$ for the left electrode and $\Gamma_{R\mu\upsilon}(E)$ for the right electrode. For such a system setup, the nonequilibrium density matrix of the scattering region is given by

$$\rho_{M\mu\upsilon} = \frac{1}{2\pi i}\int_{-\infty}^{\infty}G^<_{M\mu\upsilon}(E)\,dE, \quad (13)$$

where the additional subscript M indicates that the orbital indices μ,υ run only over the basis set functions localized in the scattering region. $G^<_{M\mu\upsilon}(E)$ is the energy- and voltage-dependent lesser Green's function for the scattering region and is given by

$$G^<_{M\mu\upsilon}(E) = \sum_{\alpha\beta} iG_{M\mu\alpha}(E)[f_L(E)\Gamma_{L\alpha\beta}(E) + f_R(E)\Gamma_{R\alpha\beta}(E)]G^\dagger_{M\beta\upsilon}(E). \quad (14)$$

As for the equilibrium case [Eq. (8)], it is then straightforward to show that $\Omega_{\mu\upsilon}$ is calculated with an analogous equation to the one used to obtain $\rho_{\mu\upsilon}$ [i.e., Eq. (13)] but that the integrand is now multiplied by the energy E:

$$\Omega_{M\mu\upsilon} = \frac{1}{2\pi i}\int_{-\infty}^{\infty}EG^<_{M\mu\upsilon}(E)dE. \quad (15)$$

Although both $\rho_{M\mu\upsilon}$ and $\Omega_{M\mu\upsilon}$ depend on the charge density of the entire infinite open system (extended molecule plus leads), they can be calculated by using just the Hamiltonian of the scattering region and the self-energies of the leads, which also set the appropriate open boundary conditions. At zero bias, Eqs. (13) and (15) are equivalent to Eqs. (7) and (8), once these are evaluated only over the basis indices running over the scattering region.

The scheme for calculating current-induced forces discussed up to this point has been implemented into the Smeagol code. Before going through a few examples, demonstrating our ability of performing structural relaxation at finite bias, we report some technical details of the implementation. In general, to ensure a smoother convergence of the charge density, we always attach at each side of the scattering region one principal layer (unit cell) of the leads. Then, when performing structural relaxation, the atoms of such principal layers are always kept fixed at their equilibrium positions (the ones of the bulk crystal). At zero bias, our formalism allows us to calculate the projection of the total energy onto the scattering region, just like in a standard ground state DFT calculation, because this ultimately depends only on $\rho_{M\mu\upsilon}$ and $H_{M\mu\upsilon}$. At finite bias, a

total energy is not defined, especially because the forces might not be conservative.[7,42]

Under current flow conditions, the density matrix of the scattering region responds to the applied bias, producing a redistribution of the electron density at the surface of the electrodes and inside the atomic junction itself (typically a molecule). The charge density accumulation at the surface of the electrodes generates an electric field, similarly to what happens in a parallel-plate capacitor. As a consequence, there is a force of purely electrostatic nature (also denoted as "direct force"[47]) originating from the charge accumulation at the surface of the electrodes and acting on the ions located between the two surfaces. In contrast, the local change in the charge density of the bridging molecule itself gives rise to a second contribution to the current-induced forces, which we refer to as wind force (the force described as originating from the continuum wave functions in Ref. 47). In literature the term "wind force" often refers to the force originating purely from the momentum transfer from the electrons to the ions;[48,49] here, we also include the forces originating from current-induced charge density rearrangements into the wind force, because these are ultimately caused by the electron flow (wind). For a given device, it is then interesting to analyze the direct force and wind force independently.

Unfortunately, purely electrostatic and wind forces are not observable separately, so it is not formally possible to distinguish between the two. If we assume that there is rather small bias-induced charging of individual atoms in the bridging molecule, then we can use an approximate procedure.[47,48] First, for fixed structure and fixed bias voltage, the total force $\vec{F}[\rho_{\mu\upsilon}(V); H_{\mu\upsilon}(V)]$ is calculated. Then an approximation for the electrostatic force can be obtained by calculating the forces for the equilibrium zero-bias charge density and the corresponding Hamiltonian, to which we add a potential shift $\Delta H_{\mu\upsilon}$. Such a shift describes an electrostatic potential offset between the two electrodes equal to V and a linear potential drop within the scattering region (as expected for a parallel-plate capacitor). Technically, $\Delta H_{\mu\upsilon}$ is obtained by adding to the Hamiltonian of the left and right leads the corresponding overlap matrix multiplied by $+eV/2$ and $-eV/2$, respectively, and a linear potential drop in the scattering region; i.e., $\Delta H_{\mu\upsilon}$ describes a position-dependent shift of the matrix elements of the Hamiltonian of the scattering region due to the electric field. We can then define the electrostatic force $\vec{F}_{\text{Field}}(V)$ as

$$\vec{F}_{\text{Field}}(V) = \vec{F}[\rho_{\mu\upsilon}(0); H_{\mu\upsilon}(0) + \Delta H_{\mu\upsilon}(V)]. \quad (16)$$

Then the wind force $\vec{F}_{\text{Wind}}(V)$ is simply obtained by subtraction as

$$\vec{F}_{\text{Wind}}(V) = \vec{F}[\rho_{\mu\upsilon}(V); H_{\mu\upsilon}(V)] - \vec{F}_{\text{Field}}(V). \quad (17)$$

Clearly, this definition is only operational, and it is not applicable in general (e.g., when the charge density is severely distorted by the bias). However, by using this simple separation, we can often provide a reasonable estimate of the two contributions and understand which force dominates in a particular device (see Sec. V).

III. FORCES FOR SYSTEMS WITHOUT CURRENT FLOW

As a first test for our methodology, in this section we present a set of calculations for systems that have no current flow. Our aim is to compare forces calculated with the NEGF scheme implemented in Smeagol (open boundary conditions) to those obtained from a DFT ground state calculation using periodic boundary conditions (PBCs), as performed with Siesta. To compare results at finite bias (but still with no current), we consider a capacitor setup, where the two electrodes are so well separated that they do not electronically interact with each other.

A. Atomic forces at equilibrium: one-dimensional Au monatomic chain

Our first goal is to verify the validity of the Green's function approach in calculating the energy density matrix at zero bias [Eq. (8)] in a practical situation. To achieve this goal, we choose a simple and idealized one-dimensional (1D) system, where the scattering region consists of a gold chain of nine atoms connected to 1D gold electrodes. The lattice spacing is assumed to be uniform at 2.8 Å, with the leads' unit cell containing two atoms. We then shift the middle Au atom in the scattering region by 1 Å in the direction transverse to the chain [Fig. 1(a)] so that a rather large restoring force is expected. In Fig. 1(b), we present the calculated forces, where the solid (black) lines represent those obtained with a standard Siesta calculation for a system periodic in the z-direction, whereas the dashed (red) lines represent the forces obtained by using our NEGF scheme. All forces are distributed so that the shifted atom is pulled back into the chain, and there is essentially no difference between the two methods. This confirms that the NEGF-calculated charge density is basically

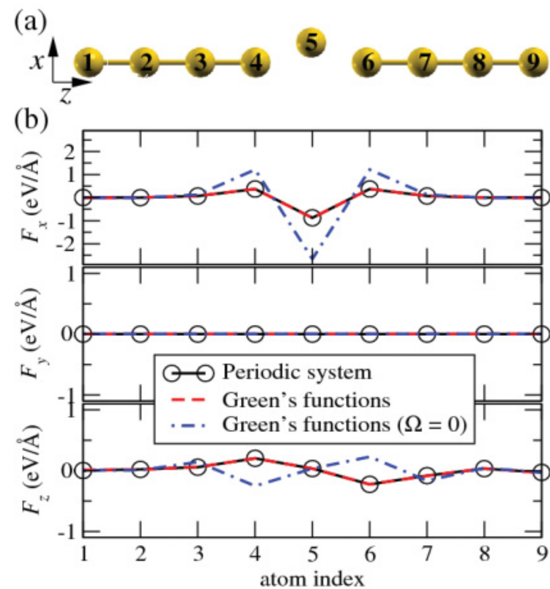

FIG. 1. (Color online) Zero-bias test for the atomic forces calculated from the NEGF scheme. (a) The system investigated is a linear Au chain, where one atom has been displaced from the chain axis. (b) We show the x-, y-, and z-components of the atomic forces acting on these nine Au atoms.

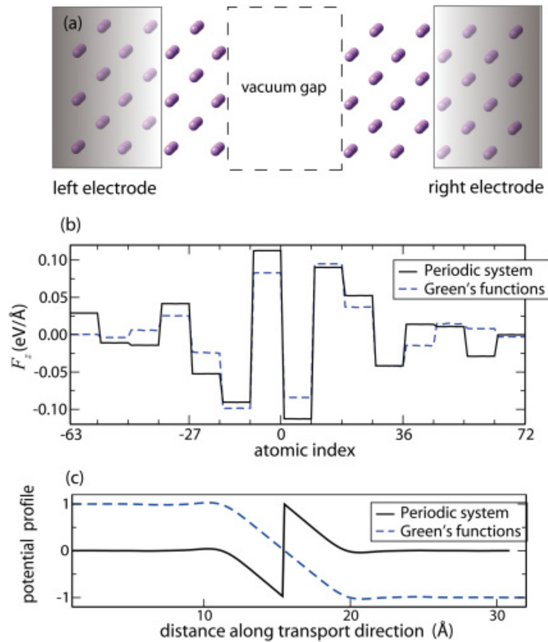

FIG. 2. (Color online) Zero-bias test for the forces acting on a parallel-plate capacitor. (a) Schematic representation of the system investigated, i.e., a parallel-plate capacitor composed of two semi-infinite Li bulk electrodes separated by 10-Å-long vacuum gap. (b) Atomic forces acting on every atom calculated with both Smeagol and Siesta at zero bias. (c) Planar average of the electrostatic potential for the system in (a) when a voltage of 2 V is applied.

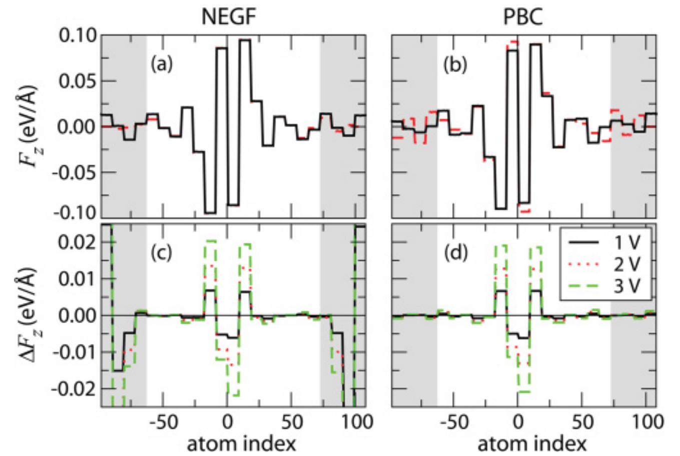

FIG. 3. (Color online) Finite- and zero-bias tests for the field-induced forces acting on a parallel-plate Li capacitor as a function of the number of atomic layers included in the simulation cell. (a) and (b) The forces at zero bias for the system in Fig. 2(a), where four (dashed red lines) and eight (solid black lines) additional Li layers have been added to each electrode. (c) and (d) The bias-induced change in the force for different bias voltages (this is the difference between the forces at zero and those at finite bias). Panels (a) and (c) show results obtained using the NEGF formalism, whereas the results in (b) and (d) are obtained by using PBC and an equivalent applied electric field.

identical to that calculated with standard DFT and PBC and that the equilibrium $\Omega_{M\mu\upsilon}$ is calculated correctly by Eq. (15). To emphasize further the importance of calculating $\Omega_{M\mu\upsilon}$ correctly, we show in Fig. 1(b) the results for forces obtained by setting $\Omega_{M\mu\upsilon} = 0$ using the dash-dotted (blue) lines. These are considerably larger, and for some atoms they even point in the wrong direction.

B. Field-induced forces over the surface atoms of the electrodes

To evaluate the accuracy of the calculated forces at finite bias, we now consider a parallel-plate capacitor that consists of two semi-infinite Li electrodes separated by a 10-Å-long vacuum gap [Fig. 2(a)]. Each atomic layer contains nine atoms, and we use 4×4 k-points in the x-y plane to account for PBCs in the orthogonal direction. There are four atomic layers in each lead unit cell. Fig. 2(c) shows the planar average in the x-y plane of the difference between the electrostatic potential at finite and that at zero bias (dashed blue line) for a voltage of 2 V. Because the vacuum region electronically disconnects the two electrodes, the same calculation can be performed as a ground state PBC calculation with an electric field applied along the z-axis (solid black line). The discontinuity in the applied sawtoothlike potential is located in the middle of the vacuum region and therefore does not affect the charge density. The figure shows that at self-consistency the planar average of the potential is flat in the metal, whereas the field-induced drop is located in the vacuum region. The resulting charge density for this system, and therefore the forces, should be approximately equal across the two methods.

We start our analysis of the forces by discussing again the zero-bias case presented in Fig. 2(b). In the figure, the atoms are sorted in the z-direction: a negative index indicates an atom located in the left electrode, whereas positive indexes are for those in the right electrode. Atom 0 is the rightmost atom of the left electrode. Although both methods yield a similar trend, there are some nonnegligible quantitative differences. Within the NEGF approach, the forces acting on the atoms at the boundary of the scattering region are expected to be somewhat inaccurate, because it is the location where the scattering region is joined to the bulk semi-infinite leads. However, this does not pose a problem, because the boundary atoms belong to those lead principal layers that in Smeagol are always kept fixed at their bulk positions. More worrying is that some forces are different at the electrode surface, where atomic relaxation should be performed. To investigate the origin of this discrepancy in detail, we calculated the forces for the same system but added four [dashed red lines in Fig. 3(a) and 3(b)] and eight [solid black lines in Fig. 3(a) and 3(b)] additional Li atomic layers at each side of the scattering region. The NEGF calculation returns to us forces that are almost constant with the length. This reflects how the present calculations effectively concern only two semi-infinite leads so that the number of layers inside the scattering region should not affect the result. In contrast, the forces calculated with PBC converge toward the NEGF result only as the electrodes get longer. This demonstrates that the forces are basically identical within the two methods, as long as a sufficiently large number of atomic layers are included in the PBC calculation. It also shows that finite size effects are smaller in the NEGF approach than in the PBC calculations. As such, we believe that our open boundary condition approach constitutes an important calculation platform for studying

surface reconstruction, because it naturally includes the correct boundary conditions, in contrast to the standard periodic calculations for a finite slab.

We now move on to analyze the forces calculated with the NEGF scheme at finite bias. These are presented in Fig. 3(c), where we display the difference between the forces at finite and those at zero bias plotted as a function of the atomic position (in practice the atomic index). The same quantity is shown in Fig. 3(d) for a PBC calculation with an equivalent applied electric field. The most notable feature is the presence of spurious NEGF-calculated forces on the atoms at the boundary of the unit cell. This is because at finite bias Smeagol introduces a potential step at this boundary, which results in a spurious contribution to the forces. Again, this only affects the peripheral atoms of the leads, i.e., those that are not relaxed. In the center of the scattering region, the charge-induced change in the forces is basically identical when calculated with the two methods. This confirms the correctness of Eq. (15). The field-induced forces at the electrode interface layers, which have been discussed in this section, are expected to produce the main contribution to the finite-bias relaxation of the metal-insulator interface in tunnel junctions, where the currents are usually very small.[50,51]

IV. CURRENT-INDUCED FORCES IN Al NANOWIRES

So far, we have only investigated systems in which there is no current flow. In this section, we present results for current-induced forces and the associated bias-induced structural instabilities. In the last decade, there have been a number of calculations on current-induced forces in metallic nanowires,[3,4,15,20,28,41,52,53] so a few theory benchmarks exist. To test our implementation, we decided to investigate the forces acting over a 4-atom-long, straight Al wire, a system that was previously discussed by Yang *et al.*[20] In Yang *et al.*'s work, the forces as a function of bias were calculated for Al wires of different lengths connected to jellium leads. In our simulation, we attach the 4-atom-long Al chains to the hollow sites of flat Al(111) electrodes. These contain nine Al atoms per plane, and we include in the scattering region five atomic layers on each side of the wire [Fig. 4(a)]. The equilibrium bond lengths are found by first relaxing the structure of a straight infinite Al monatomic wire and then by minimizing

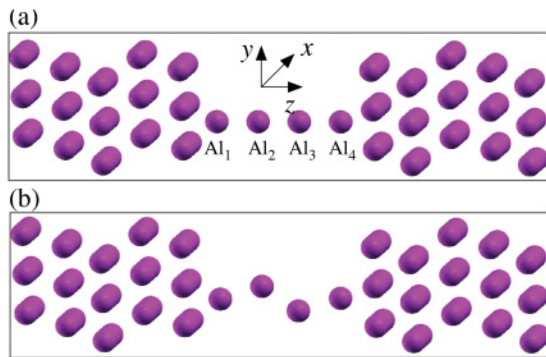

FIG. 4. (Color online) Schematic representations of the atomic structure of the (a) straight and the (b) zigzag 4-atom-long Al wires anchored to Al electrodes investigated here.

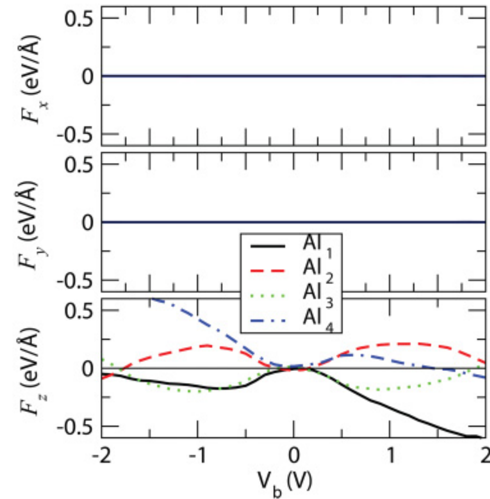

FIG. 5. (Color online) Forces as a function of the applied bias voltage acting on a 4-atom-long Al wire with a straight configuration [see Fig. 4(a)]. The forces are not zero only in the wire z-direction.

the bond length between a finite 4-atom-long chain and an Al slab. The second electrode is added symmetrically.

Once the cell is constructed, we then further relax the 4-atom-long wire while keeping the electrodes atoms fixed. The final relaxed bond lengths are 2.46, 2.45 and 2.46 Å for the first, second and the third bond in the wire, respectively, and the wire-to-surface distance is 2.02 Å. In Ref. 20, the relaxed Al-Al bond length is uniform and equal to 3.069 Å. In all calculations presented here, we use a single-ζ plus polarization basis set as control tests employing a basis of a double-ζ plus polarization quality give essentially identical results (both at zero and at finite bias). The real space mesh cutoff is equal to 400 Ry, and 4×4 k-points are used in the x-y plane. To obtain correct results for the forces at finite bias under current flow conditions, it is not possible to avail ourselves of time-reversal symmetry in the x-y plane, so we need to sample the full Brillouin zone.

In Fig. 5, we show the calculated forces as a function of bias for the straight 4-atom-long Al chains. These can be compared with those reported in Fig. 1 (d) of Ref. 20 for bias values ranging between -1 and 0 V (positive bias in Ref. 20 corresponds to negative bias in our calculations). In general, we find good agreement with the previously published results—except for the forces acting on atom 3, which are somehow different from those of Ref. 20. However, the differences are not significant and can be easily accounted for by the different leads used in the two calculations and by the consequent different initial bond lengths. Different atomic configurations result in slightly different charge distributions, and these play an important role in determining the current-induced forces.

We then perform structural relaxations of the atoms in the chain under bias and find little change in the atomic structure for bias voltages down to -3 V (we apply negative bias for the structural relaxations to be consistent with the bias direction used in Ref. 20). A similar result was found previously for Au wires.[52] The reason for this seemingly very large stability of the chain structure under bias has to be found in the somehow artificial setup of the perfectly straight chain. This causes the

forces along the x- and y-axes to vanish almost exactly. In our calculations, the x- and y-components of the forces are $<10^{-3}$ eV/Å at zero bias and remain approximately constant for all voltages (Fig. 5).

The forces vanish in the x-y plane due to an approximate rotational symmetry of the wire about the z-axis. In general, symmetries relate the forces on the different atoms. If we denote the position of the midpoint of the bond between Al_2 and Al_3 as x_0, then the system is symmetric under reflection across the x-y plane passing for x_0. Therefore, we have the following symmetry relations: $F_x(V_b,Al_1) = F_x(-V_b,Al_4)$, $F_y(V_b,Al_1) = F_y(-V_b,Al_4)$, and $F_z(V_b,Al_1) = -F_z(-V_b,Al_4)$. The system is also approximately symmetric under rotations about the x-axis, with a rotation center at x_0. This additional symmetry implies $F_x(V_b,Al_1) = F_x(-V_b,Al_4)$, $F_y(V_b,Al_1) = -F_y(-V_b,Al_4)$, and $F_z(V_b,Al_1) = -F_z(-V_b,Al_4)$. Mirror and rotation symmetry can only be fulfilled at the same time with $F_y(V_b,Al_1) = F_y(V_b,Al_4) = 0$. If we also consider the rotation symmetry around the y-axis with a rotation center at x_0, we obtain in an analogous way $F_x(V_b,Al_1) = F_x(V_b,Al_4) = 0$. The same can be shown for atoms Al_2 and Al_3. From Fig. 5, we can see that for the remaining force in the z-direction we indeed have $F_z(V_b,Al_1) \approx -F_z(-V_b,Al_4)$ and $F_z(V_b,Al_2) \approx -F_z(-V_b,Al_3)$. Again, to obtain a zero force in the x-y plane for all bias voltages, it is important to sample the k-points over the entire x-y Brillouin zone.

To study the effects of the current-induced forces on a more realistic wire structure, we perform additional structural relaxation at zero bias, this time by initializing the atomic coordinates of the two central atoms slightly off the wire axis. Interestingly, the final relaxed structure presents a zigzag shape [Fig. 4(b)], with the zigzag plane mainly oriented along the y-axis (there are also small shifts along the x-axis), so the system is approximately symmetric under rotation about the x-axis at x_0. This new structure has a total energy lower than that of the straight configuration, in agreement with previous studies.[54]

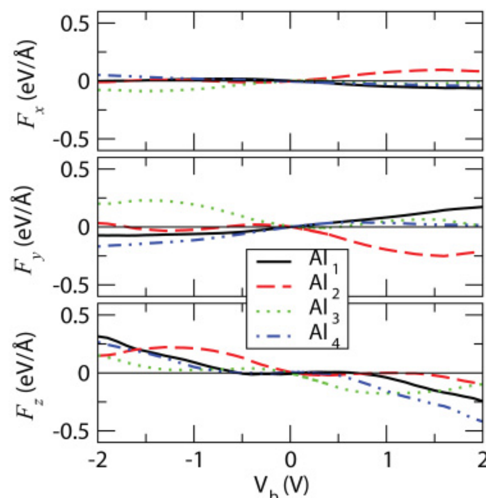

FIG. 6. (Color online) Forces as a function of the applied bias voltage for a 4-atom-long Al monatomic chain with a zigzag configuration [see Fig. 4(b)]. The forces are significant only in the zigzag plane (y-z plane).

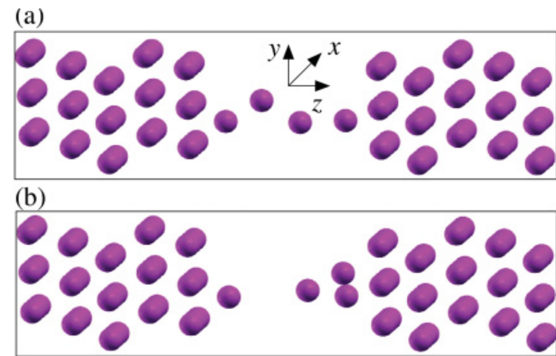

FIG. 7. (Color online) Relaxed structures at (a) $V_b = -0.2$ V and (b) $V_b = -1.4$ V obtained as the bias voltage increases from the original zigzag atomic configuration of Fig. 4(b).

In Fig. 6, the bias-dependent forces acting on the atoms of the zigzag chain are shown. These are qualitatively different from those presented in Fig. 5 for the straight wire, because now there are large forces in all directions. In particular, the forces lie mainly in the plane spanned by the zigzag chain, whereas they are small in a direction perpendicular to the plane. This feature reflects well the approximate reflection symmetry across such a plane. In addition, the forces in the z-direction are substantially different from the ones calculated for the straight chain.

We then perform structural relaxations under bias for the zigzag setup and find dramatic changes in the structure as the voltage increases. Already for $V_b = -0.2$ V, there is a transition to a different zigzag configuration, in which one atom only now lies off the z-axis [Fig. 7(a)]. As the voltage is further increased, we observe rather small but continuous changes in the structure. Finally, at -1.4 V there is a new discontinuous structural change, which effectively corresponds to the wire breaking [Fig. 7(b)]. This final structure does not get modified any longer by any voltage increasing down to -3 V. A wire breaking voltage of -1.4 V is in rather good agreement with the experimentally found breaking voltages for Au and Ir nanowires.[55] For Al nanowires, no such experimental data are available; however, in Ref. 56 the lifetime of Al wires is shown to decrease approximately linearly with bias above 0.3 V, but it is still rather large up to 0.8 V. Because we do not consider local current-induced heating in our simulations, the calculated break voltage of the wire corresponds to the voltage at which the energy barrier for the breaking process becomes zero, which corresponds to a vanishing life time in experiments. By extrapolating the experimental data for the lifetime as a function of bias, shown in Fig. 7 of Ref. 56, we might estimate the experimental lifetime to vanish ~1.6 V. A further detailed study of the breaking and of the electromigration phenomenon in Al nanowires with more realistic junction geometries, such as those discussed in Refs. 57–59, will be presented elsewhere.

Finally, in Fig. 8, we discuss the effects produced by the structural relaxation on the electron transport properties of the wires. In particular, we compare the I-V curves for both the straight and the zigzag configurations obtained with static geometry and by relaxing the structure under bias. For the straight chain, the current is almost insensitive to structural relaxation because the atoms themselves move little.

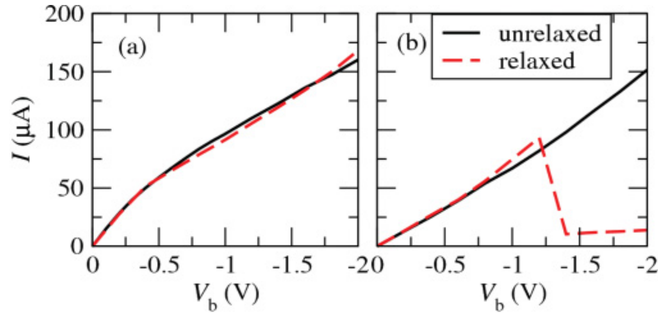

FIG. 8. (Color online) Current as a function of the bias voltage for the (a) straight and (b) zigzag configurations. The solid (black) line corresponds to calculations performed at fixed geometry, and the dashed (red) curves are obtained by relaxing the geometry at each bias voltage.

However, the situation is different for the zigzag configuration. Interestingly, the first structural transition at −0.2 V does not affect the current, because both the geometries across the transition correspond to similar zigzag wires [cf. Figs. 4(b) and 7(a)]. At −1.4 V, however, there is a drastic decrease of the current due to the wire breaking. If we take the van der Waals radius of Al, equal to 1.84 Å, as the radius of the Al monoatomic chain, we can estimate its cross section to be ∼10 Å^2. The critical current density for the wire breaking is then calculated to be $\sim 9.6 \times 10^{10}$ A/cm^2, in good agreement with the measured value[60] of 5×10^{10} A/cm^2. Furthermore, at this point, the transport changes from ballistic to tunneling, with the residual bonding interaction being responsible for the nonzero current.

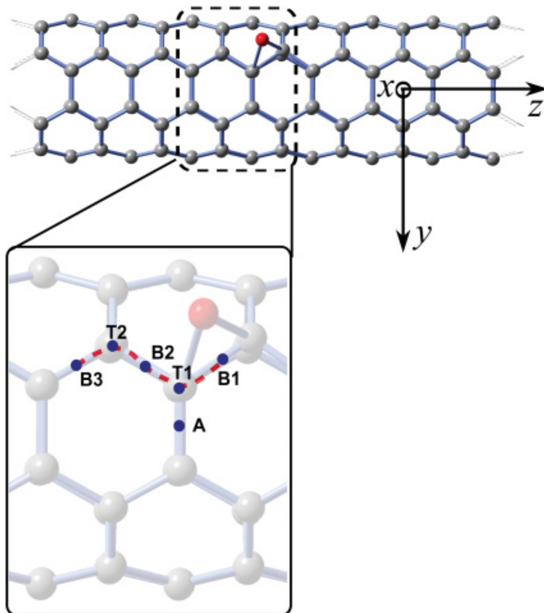

FIG. 9. (Color online) Schematic representation of an infinite (4,4) SWCNT with one Si atom sidewall attached at the B1 site. The close-up shows the diffusion path of the Si atom from the B1 to B3 site (dashed red line). The adsorption site A is also represented.

V. ELECTROMIGRATION OF A Si ATOM ON (4, 4) SWCNT

Carbon-based integrated circuits might be used as a complementary technological platform for silicon-based microelectronics.[61–63] For instance, carbon nanotube (CNT) interconnects were successfully employed to bridge on-chip silicon transistors in realistic operational environments.[62,63] It is therefore desirable to explore the effects of current-induced forces over the electromigration of Si impurities on SWCNTs. In the last decade, many theoretical studies have focused on calculating current-induced forces for single atomic small impurities (B, C, N, O, and F) and alkali metal species sidewall adsorbed on CNTs.[22,23,64] To our knowledge, however, the possibility of electromigration has never been explored before. Here, we present a series of calculations for the (4,4) metallic SWCNT incorporating a single silicon atom sidewall adsorbed at the bridge position. By means of extensive optimization, a user-defined double-ζ plus polarization basis set is constructed both for C and Si. We use an equivalent mesh cutoff of 400 Ry for the real space grid, and the cell simulation dimensions are set to be 20.0, 20.0, and 19.846 Å, respectively, in the x-, y-, and z-directions (the transport direction is z). The initial relaxed atomic structure of a (4,4) SWCNT composed of 16 layers of carbon atoms (Fig. 9) is obtained by conjugate gradient relaxation until any atomic force is <0.03 eV/Å. The lead unit cell contains 4 layers, with each layer comprising eight C atoms. For this first calculation, the leads are also (4,4) SWCNTs. Two stable independent adsorption sites at the bridge position are determined by structural relaxations at zero bias. These are indicated as the A site (Si_A) and the B1 site (Si_{B1}) in Fig. 9. The difference between the two bonding sites is that the A site lies on a C-C bond perpendicular to the tube axis and therefore perpendicular to the transport direction, whereas the B1 site is on a bond slanted from the tube axis.

For both configurations, we calculate the I-V curves up to a voltage of 1.5 V; at the same time, we relax the structure at each bias step. We find that Si_{B1} already starts to dramatically migrate along the SWCNT at the rather low threshold bias of 0.5 V (with a current of ∼60 μA). Because we do not include in our calculations the ionic vibrations caused by local heating, the migration of Si_{B1} in our structural relaxation indicates a vanishing energy barrier along the migration path at 0.5 V. The migration path essentially involves positioning the Si atom alternatively at B1 positions and on top of C atoms (see path B1 → B3 in Fig. 9). In contrast, Si_A remains almost still for all bias voltages considered. An analysis of current-induced forces at finite bias indicates that the force acting on Si_A along the C-C bond (the y-axis) is negligible; therefore, the Si_A atom does not move. In contrast, for Si_{B1} there is a substantial force along the C-C bond because it lies along the current flow. This causes migration at low bias.

To understand the nature of the current-induced forces acting on Si, we decompose them into the two components described at the end of Sec. II: the electrostatic component and the wind component (the total force is equal to the sum of the two). These are shown in Fig. 10 for both Si_A and Si_{B1} as a function of bias. As expected, the electrostatic force increases approximately linearly with bias, but it is rather small for both Si positions. This is because the electric field is rather weak along the long CNT considered and because the Si adatom

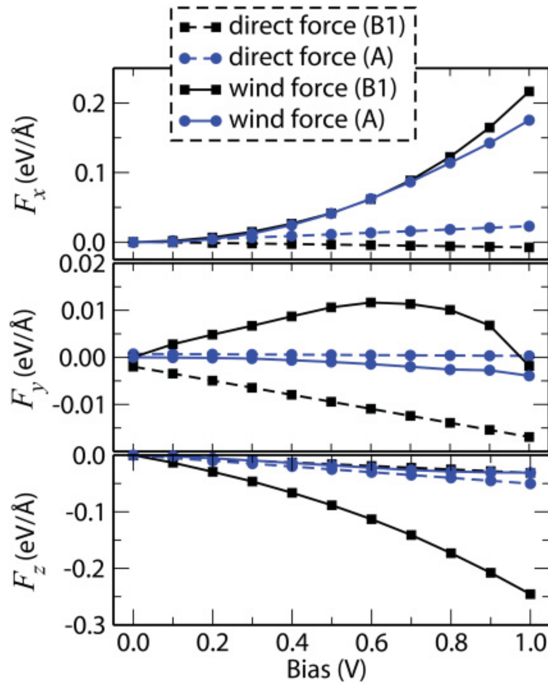

FIG. 10. (Color online) The current-induced forces acting on the Si adatom as a function of bias are decomposed into electrostatic forces and wind forces in the three Cartesian directions [see Eqs. (16) and (17)].

is almost in a charge neutral state. Furthermore, to confirm the small contribution made by the electrostatic forces, we calculate the electrostatic forces for both the Si_A and the Si_{B1} adatoms by using Siesta, where an electric field is applied along the tube axis, for a CNT of finite length. The results show that the electrostatic forces in both cases are negligibly small. In contrast, the wind force for the Si_{B1} atom is large, so in this case it almost coincides with the total force. We can then conclude that the wind force is responsible for the electromigration of Si_{B1}.

Interestingly, for Si_A there is a significant wind force acting in the x-direction, i.e., in the CNT radial direction. However, Si_A is tightly bound to the CNT in the radial direction and therefore does not move. We note however that the atom changes its position significantly away from the CNT. A significant radial current-induced force should result in a measurable change in the desorption barrier height. This can indeed be measured in a scanning tunneling microscopy experiment. Finally, the z-component of the wind force acting on Si_A is much smaller than that acting on Si_{B1}. Because the wind force depends on the current-induced electron charge redistribution around the given scattering center, we might expect that such redistribution will be small if there is a small current along a bond.

To verify this hypothesis, we calculate the bond current for the two configurations. The bond current between two orbitals $J_{\mu\upsilon}$ is obtained as[65–67]

$$J_{\mu\upsilon} = \frac{2e}{h}\int_{-\infty}^{\infty}[H_{\mu\upsilon}G^{<}_{M\upsilon\mu}(E) - H_{\upsilon\mu}G^{<}_{M\mu\upsilon}(E)]dE, \tag{18}$$

whereas that between two atoms with indices I and K, or the bond current J_{IK}, corresponds to the sum of the bond currents between individual orbitals located at those atoms, or

$$J_{IK} = \sum_{\mu\in I,\upsilon\in K} J_{\mu\upsilon}. \tag{19}$$

Furthermore, the total bond current acting on an individual atom can be represented in vectorial form as

$$\vec{J}_I = \sum_{K\neq I} J_{IK}\vec{\upsilon}_{IK}, \tag{20}$$

where $\vec{\upsilon}_{IK}$ is the vector connecting atoms I and K. The calculated bond currents for a bias voltage of 1 V are shown in Fig. 11. In the figure, the thick arrowhead (black) lines represent the current vector acting on an atom according to Eq. (20). First, we show the bond currents for an infinite and defect-free (4,4) SWCNT [Fig. 11(a)] and find that the current flow is mainly along the longitudinal C-C bonds (the one along the SWCNT axis), with the transverse component vanishing. We then evaluate the bond currents for the SWCNTs with the Si adatoms. The presence of Si_A perturbs only marginally the bond currents acting on the C atoms, which closely resemble those of the defect-free SWCNT [Fig. 11(b)]. This means

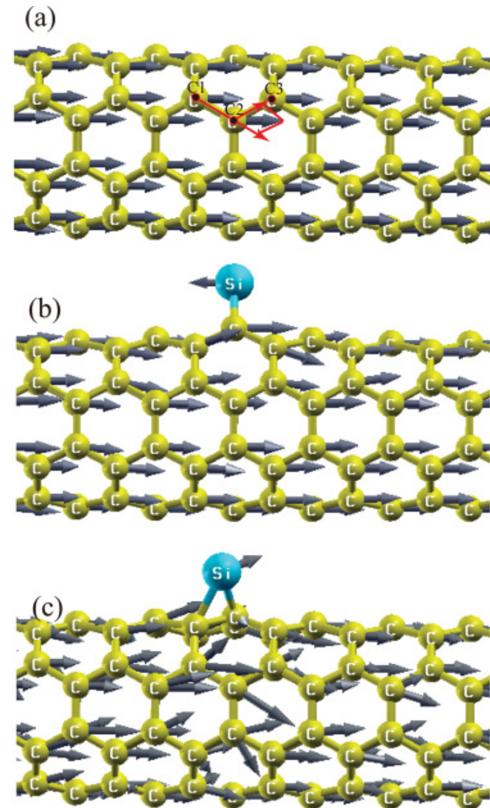

FIG. 11. (Color online) Schematic pictures of bond-current distribution in three systems at the bias voltage of 1 V: (a) an infinite and perfect (4,4) SWCNT, (b) an infinite (4,4) SWCNT with Si_A, and (c) an infinite (4,4) SWCNT with Si_{B1}. The thin arrowhead (red) lines in (a) illustrate that the total current vector on each C atom is mainly given by a sum of the bond-current vectors from its two longitudinally neighboring C atoms; thus, the transverse component in the total current vector vanishes.

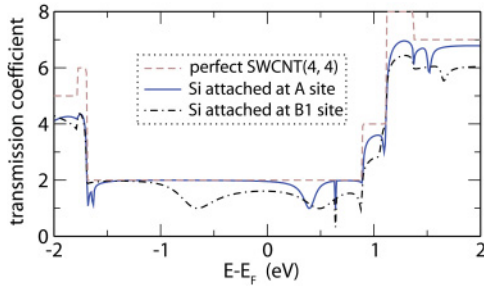

FIG. 12. (Color online) Zero-bias transmission coefficients as a function of energy for the three systems illustrated in Fig. 11: an infinite and perfect (4,4) SWCNT and an infinite (4,4) SWCNT with either Si_A or Si_{B1}.

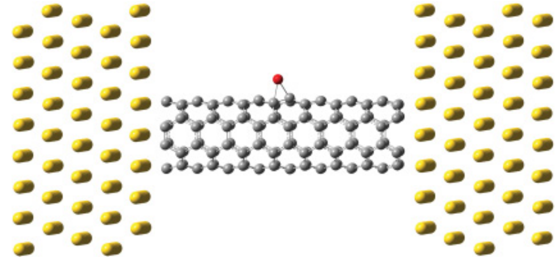

FIG. 13. (Color online) Two-terminal device constructed by attaching a SWCNT to two Au electrodes. The SWCNT includes a Si_{B1} adatom. This is equivalent to the device geometry of Fig. 9, except that the SWCNT leads in that figure are replaced by Au here.

that Si_A acts as a weak scattering center, i.e., it is off the current flow. Small bond currents between the Si atom and its neighboring C atoms result in a total bond current on Si_A pointing against the overall current flow. No currents pass across the transversal C-Si-C bonds either from C to Si or from C to C atoms, and this explains why the y-component of the force is very small. In contrast, Si_{B1} lies in the current flow path and therefore acts as a strong scattering center [Fig. 11(c)]. As a result, the current on the SWCNT atoms significantly changes as compared to the case of the perfect SWCNT. This time, there is a large bond current along the C-Si-C bonds and consequently a large z-component of the wind force.

Further support to our analysis of the scattering properties of the two Si adsorption centers is provided by comparing the difference between the corresponding zero-bias transmission coefficients (Fig. 12). For Si_{B1}, there is a reduction in transmission around the Fermi energy (E_F) significantly larger than that produced by Si_A. This is fully consistent with the previous finding that Si_{B1} is a stronger scattering center than Si_A.

So far we have performed calculations for an infinite metallic (4,4) SWCNT with a single Si scatterer (this means that both the scattering region and the leads are formed by the same SWCNT). Clearly, this does not correspond to a completely physical situation at finite bias, because in our setup the potential imposed over the scattering region cannot be screened completely at the boundary with the leads.[68] Therefore, to verify whether or not the results presented in this section depend on these (artificial) boundary conditions, we set up a separate calculation, where the SWCNT is now attached to two Au electrodes. In this case, the finite-bias potential is fully screened by Au. The unit cell used for the Si_{B1} case is shown in Fig. 13, and it is identical to the one used for Si_A. The results obtained for the infinite SWCNT are fully preserved; i.e., Si_A does not move at any bias, whereas Si_{B1} will migrate if the applied voltage is sufficiently large. The critical bias for the migration is now 0.8 V. This result is expected, because the addition of two CNT/Au interfaces introduces a supplementary contact resistance (the current at the critical voltage for migration is ~45 μA). The distribution of the bond currents around the Si adatom at 0.8 V is similar to that at 0.5 V for the infinite SWCNT case, indicating again that all action is due to the large wind force.

Before concluding this section, we analyze the effects of the Si adatom diffusion on the transport properties. We perform a structural relaxation for Si_{B1} at $V_b = 0.5$ V and calculate the current at each conjugate gradient step. The resulting simulated steady-state current behaves in an oscillation form, reflecting the diffusion of the Si_{B1} atom along the B1 to B3 path (see Fig. 9). Our calculation reveals that the five turning points of the simulated current correspond to the specific atomic positions indicated in Fig. 14(a). The transient current for adsorption at the bridge site is ~50% larger than that for the top site. Finally, we calculate the energy-dependent transmission coefficients at 0.5 V for Si positioned on two selected locations along the migration path: the B2 and T1 sites (see Fig. 9). The results are shown in Fig. 14(b). The transmission for adsorption at T1 is significantly reduced within the energy window between −0.5 and 0.5 eV when compared to that for B2 adsorption. This indicates that one of the two conducting channels incident from the nanotube lead is likely switched off near the Fermi level due to a localized impurity state around the silicon adatom.[69] From a scattering point of view, the Si adatom at the T1 position appears to be a much stronger scattering center for the current; therefore, at the considered voltage of 0.5 V, it induces a larger force. This is 0.24 eV/Å,

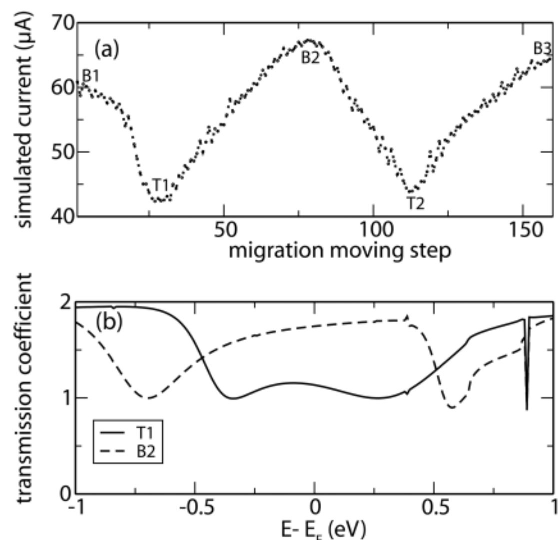

FIG. 14. (a) The current at $V_b = 0.5$ V oscillates with the Si_{B1} migration process; the characteristic transient Si bonding locations are seen as turning points. (b) Transmission coefficients at $V_b = 0.5$ V for Si adsorbed at the T1 and B2 positions (see Fig. 9).

compared to the one for B2 adsorption, which is equal to only 0.10 eV/Å.

VI. CONCLUSIONS

We presented an algorithm for evaluating current-induced forces in atomic junctions and a few applications for systems of scientific and technological interest. The algorithm naturally integrates into the NEGF + DFT framework, and it is implemented in the Smeagol code. This enables us to perform atomic relaxations out of equilibrium in the presence of an electric current and thereby investigate the interplay between structural relaxation and transport properties. The algorithm is first thoroughly tested against known results and is benchmarked against total energy calculations, whenever possible.

We then took on two systems of significant scientific interest. First, we studied current-induced forces in Al nanowires with either a straight or a zigzag configuration and discussed their bias-induced structural instabilities. We estimated a critical current density for the junction breaking rather close to the one measured experimentally. Finally, we explored the possibility for current-induced forces to manipulate the position of a Si adatom on the surface of a (4,4) metallic SWCNT. Remarkably, our calculations predict electromigration as soon as the bias voltage exceeds a certain critical value. We then demonstrated that the position-dependent wind force is the one responsible for the diffusion process. A close analysis of the transmission revealed that the wind-type current-induced forces are closely related to the local electron scattering strength.

ACKNOWLEDGMENTS

The authors thank T. Todorov for useful discussions and for a critical reading of our manuscript. This project was supported by the National Natural Science Foundation of China (Grant No. 61071012), China's Ministry of Education (Grant No. NCET-07-0014), the Ministry of Science and Technology of China (Grants No. 2007CB936204 and No. 2011CB933001) and the China Scholarship Council program. S.S. and I.R. acknowledge the Science Foundation Ireland (Grant No. 07/IN.1/I945). I.R. thanks the King Abdullah University of Science and Technology for financial support (ACRAB project). Calculations were performed within the Irish Centre for High-End Computing and on the Parsons cluster maintained by the Trinity Centre for High Performance Computing.

---

*smhou@pku.edu.cn

[1] A. Nitzan and M. A. Ratner, Science **300**, 1384 (2003).
[2] N. J. Tao, Nat. Nanotechnol. **1**, 173 (2006).
[3] T. N. Todorov, J. Hoekstra, and A. P. Sutton, Phys. Rev. Lett. **86**, 3606 (2001).
[4] M. Di Ventra, S. T. Pantelides, and N. D. Lang, Phys. Rev. Lett. **88**, 046801 (2002).
[5] Z. Q. Yang and M. Di Ventra, Phys. Rev. B **67**, 161311 (2003).
[6] C. Verdozzi, G. Stefanucci, and C. O. Almbladh, Phys. Rev. Lett. **97**, 046603 (2006).
[7] D. Dundas, E. J. McEniry, and T. N. Todorov, Nat. Nanotechnol. **4**, 99 (2009).
[8] H. Park, A. K. L. Lim, A. P. Alivisatos, J. Park, and P. L. McEuen, Appl. Phys. Lett. **75**, 301 (1999).
[9] G. Esen and M. S. Fuhrer, Appl. Phys. Lett. **87**, 263101 (2005).
[10] R. Sordan, K. Balasubramanian, M. Burghard, and K. Kern, Appl. Phys. Lett. **87**, 013106 (2005).
[11] M. W. Zheng, M. Steinacher, R. Huber, M. Calame, S. J. Molen, and C. Schonenberger, Appl. Phys. Lett. **91**, 053118 (2007).
[12] M. Araidai and M. Tsukada, Phys. Rev. B **80**, 045417 (2009).
[13] T. N. Todorov, Philos. Mag. B **77**, 965 (1998).
[14] T. N. Todorov, J. Hoekstra, and A. P. Sutton, Philos. Mag. B **80**, 421 (2000).
[15] M. Di Ventra, *Electrical Transport in Nanoscale Systems* (Cambridge University Press, Cambridge, United Kingdom, 2008).
[16] N. Agraït, C. Untiedt, G. Rubio-Bollinger, and S. Vieira, Phys. Rev. Lett. **88**, 216803 (2002).
[17] Y. C. Chen, M. Zwolak, and M. Di Ventra, Nano Lett. **3**, 1691 (2003).
[18] Z. Ioffe, T. Shamai, A. Ophir, G. Noy, I. Yutsis, K. Kfir, O. Cheshnovsky, and Y. Selzer, Nat. Nanotechnol. **3**, 727 (2008).
[19] Z. F. Huang, F. Chen, R. D. Agosta, P. A. Bennett, M. Di Ventra, and N. J. Tao, Nat. Nanotechnol. **2**, 698 (2007).
[20] Z. Yang, M. Chshiev, M. Zwolak, Y. C. Chen, and M. Di Ventra, Phys. Rev. B **71**, 041402(R) (2005).
[21] A. Safiei, J. Henzl, and K. Morgenstern, Phys. Rev. Lett. **104**, 216102 (2010).
[22] S. Heinze, N. P. Wang, and J. Tersoff, Phys. Rev. Lett. **95**, 186802 (2005).
[23] N. Mingo, L. Yang, and J. Han, J. Phys. Chem. B **105**, 11142 (2001).
[24] R. Landauer, Phys. Rev. B **14**, 1474 (1976); **16**, 4698 (1977).
[25] R. S. Sorbello and B. B. Dasgupta, Phys. Rev. B **21**, 2196 (1980).
[26] I. A. Blech and H. Sello, *Physics of Failure in Electronics*, edited by T. S. Shilliday and J. Vaccaro (USAF, Rome Air Development Center, Rome, 1967).
[27] M. Hauder, J. Gstottner, W. Hansch, and D. Schmitt-Landsiedel, Appl. Phys. Lett. **78**, 838 (2001).
[28] M. Di Ventra and S. T. Pantelides, Phys. Rev. B **61**, 16207 (2000).
[29] A. R. Rocha, V. M. García-Suárez, S. Bailey, C. Lambert, J. Ferrer, and S. Sanvito, Nat. Mater. **4**, 335 (2005).
[30] A. R. Rocha, V. M. García-Suárez, S. Bailey, C. Lambert, J. Ferrer, and S. Sanvito, Phys. Rev. B **73**, 085414 (2006).
[31] I. Rungger and S. Sanvito, Phys. Rev. B **78**, 035407 (2008).
[32] L. V. Keldysh, Sov. Phys. JETP **20**, 1018 (1965).
[33] H. Haug and A. P. Jauho, *Quantum Kinetics in Transport and Optics of Semiconductors* (Springer, Berlin, 1996).
[34] J. Ferrer, A. Martin-Rodero, and F. Flores, Phys. Rev. B **38**, R10113 (1998).
[35] P. Ordejón, E. Artacho, and J. M. Soler, Phys. Rev. B **53**, R10441 (1996).

[36]J. M. Soler, E. Artacho, J. D. Gale, A. García, J. Junquera, P. Ordejón, and D. Sánchez-Portal, J. Phys. Condens. Matter **14**, 2745 (2002).

[37]H. Hellmann, *Einführung in die Quantenchemie* (F. Deuticke, Leipzig, 1937), Sec. 54; R. P. Feynman, Phys. Rev. **56**, 340 (1939).

[38]T. N. Todorov, J. Phys. Condens. Matter **13**, 10125 (2001).

[39]T. N. Todorov, J. Phys. Condens. Matter **14**, 3049 (2002).

[40]P. Kumar and R. S. Sorbello, Thin Solid Films **25**, 25 (1975).

[41]M. Di Ventra, Y. C. Chen, and T. N. Todorov, Phys. Rev. Lett. **92**, 176803 (2004).

[42]T. N. Todorov, D. Dundas, and E. J. McEniry, Phys. Rev. B **81**, 075416 (2010).

[43]P. Pulay, *Modern Theoretical Chemistry*, edited by H. F. Schaefer (Plenum, New York, 1977), Vol. 4.

[44]O. F. Sankey and D. J. Niklewski, Phys. Rev. B **40**, 3979 (1989).

[45]E. F. Hayes and R. G. Parr, J. Chem. Phys. **43**, 1831 (1965).

[46]N. D. Lang, Phys. Rev. B **45**, 13599 (1992); **49**, 2067 (1994).

[47]M. Di Ventra and N. D. Lang, Phys. Rev. B **65**, 045402 (2001).

[48]R. S. Sorbello, Phys. Rev. B **39**, 4984 (1989).

[49]R. S. Sorbello, *Solid State Physics* (Academic Press, New York, 1998), Vol. 51, p. 159.

[50]I. Rungger, O. Mryasov, and S. Sanvito, Phys. Rev. B **79**, 094414 (2009).

[51]N. M. Caffrey, T. Archer, I. Rungger, and S. Sanvito, Phys. Rev. B **83**, 125409 (2011).

[52]M. Brandbyge, K. Stokbro, J. Taylor, J. L. Mozos, and P. Ordejón, Phys. Rev. B **67**, 193104 (2003).

[53]M. Brandbyge, J. L. Mozos, P. Ordejón, J. Taylor, and K. Stokbro, Phys. Rev. B **65**, 165401 (2002).

[54]M. Springborg and Y. Dong, Int. J. Quant. Chem. **109**, 837 (2009).

[55]R. H. M. Smit, C. Untiedt, and J. M. van Ruitenbeek, Nanotechnology **15**, S472 (2004).

[56]J. I. Mizobata, A. Fujii, S. Kurokawa, and A. Sakai, Phys. Rev. B **68**, 155428 (2003).

[57]P. Jelinek, R. Perez, J. Ortega, and F. Flores, Nanotechnology **16**, 1023 (2005).

[58]P. Jelinek, R. Perez, J. Ortega, and F. Flores, Phys. Rev. B **68**, 085403 (2003).

[59]P. Jelinek, R. Perez, J. Ortega, and F. Flores, Surf. Science **566**, 13 (2004).

[60]T. Minowa, S. Kurokawa, and A. Sakai, Physica E **29**, 495 (2005).

[61]W. Lu and C. M. Liber, Nat. Mater. **6**, 841 (2007).

[62]G. F. Close, S. Yasuda, B. Paul, S. Fujita, and H.-S. P. Wong, Nano Lett. **8**, 706 (2008).

[63]X. Y. Chen, D. Akinwande, K. J. Lee, G. F. Close, S. Yasuda, B. Paul, S. Fujita, J. Kong, and H.-S. P. Wong, IEEE Trans. Electron. Dev. **57**, 3137 (2010).

[64]Y. Girard, T. Yamamoto, and K. Watanabe, J. Phys. Chem. C **111**, 12478 (2007).

[65]A. Cresti, R. Farchioni, G. Grosso, and G. P. Parravicini, Phys. Rev. B **68**, 075306 (2003).

[66]L. P. Zârbo and B. K. Nikolić, EPL **80**, 47001 (2007).

[67]H. Nakamura, J. Phys. Chem. C **114**, 12280 (2010).

[68]Z. Qian, R. Li, S. Hou, Z. Xue, and S. Sanvito, J. Chem. Phys. **127**, 194710 (2007).

[69]H. Park, J. Zhao, and J. P. Lu, Nano Lett. **6**, 916 (2006).